
Article

INTERDIGITATED ELECTRODE FOR ELECTRICAL CHARACTERIZATION OF COMMERCIAL PSEUDO-BINARY BIODIESEL-DIESEL BLENDS

Inocência Santos Neto¹, Christian Carvalho¹, Gilberto Filho¹, Cássio Andrade¹, Allan Barros¹, João Fonseca Neto¹, Vicente Paucar¹, Luciana Alencar², Fernando Silva³ and Francisco Sinfrônio^{1,*}

¹ Department of Electrical Engineering, Federal University of Maranhão, Campus of Bacanga, São Luís, 65080-805, Brazil; netto.ufma@gmail.com.

² Department of Physics, Federal University of Maranhão, Campus of Bacanga, São Luís, 65080-805, Brazil.

³ Department of Chemistry, Federal University of Maranhão, Campus of Bacanga, São Luís, 65080-805, Brazil.

* Correspondence: netto.ufma@gmail.com

Abstract: Non-standard diesel blends can be harmful to the environment and human health. In this context, a simple analytical method to estimate the biodiesel mixture ratio in diesel was developed based on the impedance spectroscopy (IS) associated with the interdigitated sensors. In this article, four different interdigitated sensors, variable comb spacing (G), were simulated using the COMSOL Multiphysics software. Based on finite element simulations, four interdigitated electrode architectures by manufactured and evaluated. According to the X-ray powder diffraction technique, the deposition of the conductive layer (Au^o) over the surface of the dielectric substrate (SiO₂) did not alter its phase composition. In the analysis of AFM and SEM, it was possible to observe irregular edges on the electrodes, possibly related to thin layers' manufacturing process and mechanical stability. Another characteristic observed in the AFM images was the height of the step of the gold layer of the sensor. Several cross-sections were obtained, and the mean step value is 225.71 ± 0.0032 nm. Although there are differences in the roughness, the whole sensor has nanometric roughness. Based on the finite element method simulation performed, it can be assumed that the geometric parameters more suitable for the manufacturing of the electrode are: $W = 20 \mu\text{m}$, $L = 1000 \mu\text{m}$, $G = 50 \mu\text{m}$ e $N = 40$ digits. The electrical characterization performed by impedance spectroscopy showed that we could differentiate between biodiesel and diesel fuels and their pseudo-binary mixtures in the low-frequency region.

Keywords: interdigitated electrodes; pseudo binary biodiesel-diesel blends; impedance.

1. Introduction

By definition, biodiesel is a complex mixture of long-chain esters, often produced by the transesterification of vegetable oils and/or animal fats using short-chain alcohol and homogeneous or heterogeneous catalysts [1]. Due to its combustion properties and fossil-based combustible, it can be used as a fuel itself or as an additive for diesel commercial blends in several different proportions.

In Brazil, the National Petroleum, Natural Gas and Biofuels Agency (ANP) is responsible, among other things, for controlling the local commercialization of fuels as well as regulating the volume of additive added to liquid fuels such as in diesel/biodiesel pseudo-binary blends. To do so, the ANP currently recommends that all commercial diesel blends must be evaluated according to EN14078, ASTM D7371 and NBR15568 standards methodologies using near-infrared spectroscopy and multivariate analysis [2]. Despite of their extremely high operational costs, several authors have suggested the development of alternative methodologies based on chromatography analyses or nuclear magnetic resonance spectroscopy [3,4,5].

Recently, electrochemical impedance spectroscopy employing interdigitated sensors emerged as an affordable technology for evaluating the dielectric properties and chemical composition of the fuel pseudo-binary blends [6,7]. González Prieto et al., for instance, uses impedance spectroscopy for dielectric characterization of diesel and biodiesel samples, reporting room-temperature dielectric constant of 2.2 and 3.3, respectively [8]. Similar results were reported by [9].

In this context, [10,11] suggest that interdigitated electrodes can be used in association to impedance spectroscopy to predict the dielectric performance of liquid fuel samples and at a given level, correlates them to its chemical composition.

Currently, interdigitated electrodes have been used in surface acoustic wave devices [12], acoustic transducers [13], tunable devices [14], and as probes for dielectric spectroscopy [15] due to its design flexibility, reduced sizes, and affordable prices, being able to detect multiple physical properties in different frequency domains [16]. Apart from these, interdigitated electrodes have also been broadly utilized in biological and chemical sensing, in which the changes in capacitance or impedance have been gauged based on the relationship between the analyte and a sensitive layer [17].

The advantages of these devices are the miniaturization of the electrodes, low manufacturing cost, and the potential for use in a series of applications without substantial changes in the sensor design. Moreover, interdigitated electrodes, present promising advantages in terms of low ohmic drop, the fast establishment of steady-state, rapid reaction kinetics, and increased signal to noise ratio [18]. Basically, the structure includes two parallel coplanar electrodes, with periodical repetition of design (length, width, electrode spacing).

The use of interdigitated electrodes eliminates the need for a reference electrode and provides simple means for obtaining a steady-state current response. Since anodic and cathodic electrodes are put together, minute amounts of species can be analyzed between the electrodes [19].

Therefore, this work aims to evaluate the effect of the design and chemical composition of the interdigitated electrode on its sensitivity to pseudo-binary biodiesel-diesel.

2. Materials and Methods

2.1. Interdigitated electrode design by the finite element method

Computational simulation offers the possibility of exploring the sensitivity of different geometric configurations of prototypes before their manufacture. In this paper, four distinct interdigital electrodes were designed by varying combs spacing (G) and keeping the digits width (W) and digit length (L) constant (Table 1).

Table 1. Physical dimension of the interdigitated electrodes.

Sensor coding	Combs spacing (μm)	Effective area (mm^2)	Number of electrodes (units)
Ba1810	10	1.25	20
Ba1820	20	1.65	20
Ba1830	30	2.00	20
Ba1850	50	2.80	20

Each interdigitated electrode consists of a group of twenty parallel buses connected alternately to the hot (0.2 V) and ground terminals (Figure 1).

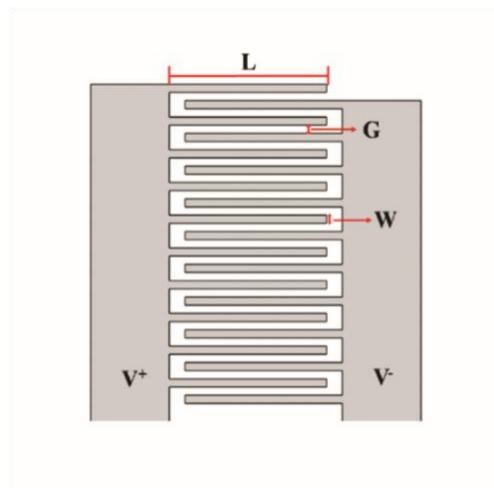


Figure 1. Two-dimensional (2D) schematic representation of the interdigitated electrodes.

The dielectric studies were performed using the electrostatics interface available on the AC/DC module of the COMSOL Multiphysics platform. Therefore, the electric field distribution, electric field magnitude, and the capacitance for each electrode were predicted employing a 3D-planar geometric model developed with 231.894 tetrahedral elements and appropriate boundary conditions.

After the finite element analysis and electrical prospecting, each interdigitated electrode (sensor) was manufactured by microelectronic photolithography process using quartz slide ($28.0 \times 5.0 \times 0.4$ mm) as dielectric substrate and metallic gold layers as conductive trails (Au^0 thickness ≈ 225 nm).

2.2. Chemical and physical characterization of the interdigital electrode

Wavelength dispersive X-ray fluorescence (WDXRF) spectra were obtained by Tiger S8 (Bruker) tube with Rhodium (Rh), which operated between 30-50 kV/20-33 mA, XS-55, PET, LiF200, XS-GE-55 crystals, and 0.23° or 0.40° collimators. Mylar[®] films (3.6 mM) also Teflon recipient were employed.

X-ray powder diffraction (XRPD) measurements were recorded using a D8 Advance diffractometer (Bruker) with a $\text{CuK}\alpha$ ($\lambda=1.5406$ Å) tube operating at 40 kV/40 mA and the LynxEye linear detector. The data were collected in Bragg-Brentano geometry, in the range of 20 to 100° , with step size of 0.02° and counting time of 0.5 s. The XRPD patterns were compared with the Joint Committee Powder Diffraction Standards (JCPDS) data for the phase evaluation.

Three-dimensional topographic images and electrode roughness analysis were performed using a Multimode 8 (BRUKER, CA) atomic force microscope with QNM (Peak Force Tapping Quantitative Nanomechanics) mode. Therefore, nominal spring constant SCANASYST-AIR (BRUKER) probes of 0.4 N.m⁻¹ and nominal tip radius of 2 nm were adopted.

The topology evaluation was carried out using a scanning electron microscope ZEISS EVO HD15, with 150 X magnification, vacuum pressure of 10^{-7} Pa, and electron acceleration voltage of 5 kV. The compositional analysis of each device was predicted by means of X-ray Dispersive Energy Spectrometry (EDX) using a Quantax/Bruker equipment.

Finally, the electrical properties of the sensors were estimated using a frequency response analyzer Solartron model 1260 in which the designed interdigitated electrodes were connected by shielded cable and BNC inputs, both with 50 Ω impedances. All measurements were carried out using 0.2 V and five points for decades, in a frequency range between 1 to 1×10^6 Hz. The measurements were performed at a temperature of 21.0 ± 0.1 °C. The whole process being computer-controlled. To minimize the effects of external interference, a conductive arrangement based on the Faraday's cage principle was used.

3. Results

3.1. Finite element analysis and electrical evaluation

According to [20], the sensitivity of any electronic sensor is dependent on its architecture. Thus, this work evaluated the influence of the number of digits, conductive layer thickness, digit width, and the distance between the digits on the Maxwell capacitance of the interdigitated electrodes.

As shown in Figure 2, all interdigitated electrodes were assembled as a coupling of adjacent conducting digits in which their general capacitance is equivalent to the sum of each capacitor created in each pair of combs. Thus, the increase in the number of conducting digits promotes a linear increase in Maxwell capacitance (Figure 2a). Similarly, the estimated Maxwell capacitance is proportional to the width of the digits in the sensor due to the edge field effect that occurs on the surface of the interdigitated electrodes.

According to [21], the large spacing between the interdigitated electrodes produces more uniform electric field lines and a more optimized strain coefficient. However, to produce an equivalent electric field with these dimensions, it would be necessary to apply higher voltages, increasing energy consumption. In contrast, a decrease in electrode spacing will make the manufacturing process more difficult and increase the likelihood of defective conductive layer paths.

According to [22], the digit width parameter must be optimized since it can lead to electrical field distortions at the conductive track edges. In interdigitated electrodes, the capacitance is given mainly by the electromagnetic interaction between the two electrodes' conductive track edges. Thus, considering a fixed-size sensor, the greater G and W , the smaller is the number of edges in the tracks of the electrodes, which reduces the value of the capacitance and hence its sensitivity. The influence of conductor metal layer thickness on the capacitance of the interdigitated electrodes was determined using the following geometry: $w = 20 \mu\text{m}$, $L = 1000 \mu\text{m}$, $G = 50 \mu\text{m}$ and $n = 40$ digits. According to [23] the electrode thickness does not influence a parallel plate capacitor's capacitance. However, in an interdigital capacitor, the electrode thickness has a discernible influence on the device capacitance. As shown in Figure 2d, such electrical property varies sigmoidal with the conductor layer due to the contribution of the air-filled capacitor.

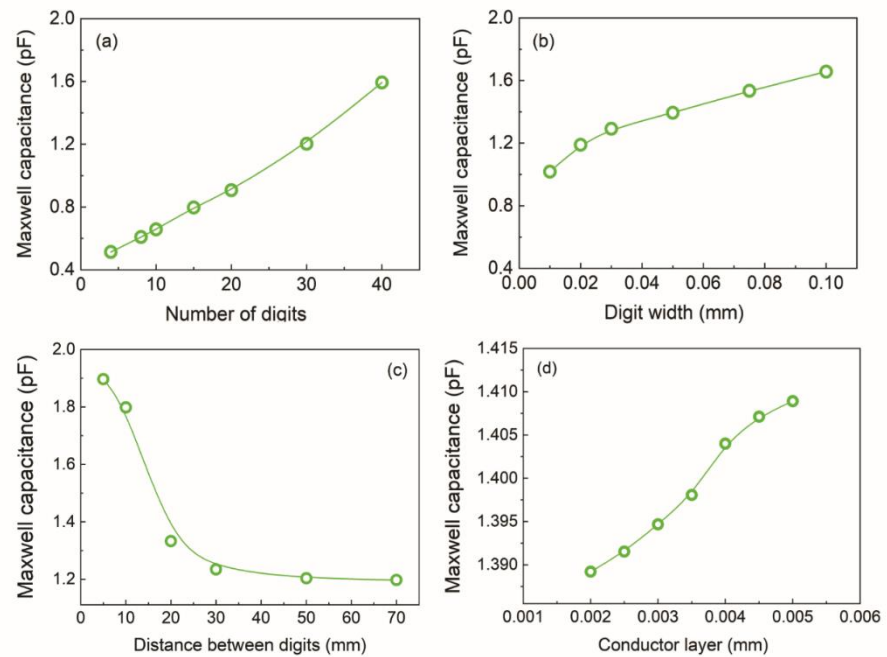


Figure 2. Maxwell capacitance as a function of the (a) number of digits, (b) digit width, (c) distance between digits, and (d) conductor layer of the interdigitated electrodes.

One of the operating principles of the interdigitated capacitive sensor used in this work is based on parallel plate capacitors. Once an AC voltage is applied between the positive and negative electrodes, electric fields are generated. If there is any material nearby, the generated electric fields penetrate the materials, which leads to changes, mainly in the capacitive reactance of the sensor, hence its impedance. [24].

According to the finite element simulation, the electric field lines generated on the interdigitated electrode surface have a “fringe-like distribution” throughout all the comb pairs (Figure 3a). Nonetheless, such electrical field lines are widely distorted when the conductive layer is enlarged, probably due to parasitic capacitive phenomena (Figure 3b).

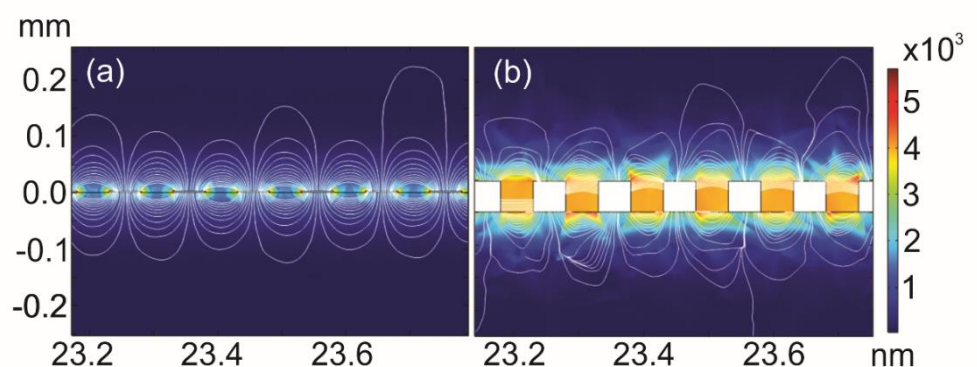


Figure 3. Electric field lines for the interdigitated electrode with (a) 0.00254 nm, and (b) 0.04754 nm.

Due to the coplanar nature of the sensor, there are more prominent fringing field lines in addition to the direct field lines between the fingers; this makes the coplanar type capacitive sensor more sensitive to the changes in the electrical properties of the surrounding medium. Therefore, by measuring the changes in the impedance, the electrochemical sensing behavior can be observed. [25].

3.2. Interdigitated electrode description

3.2.1 Structural characterization

X-ray diffraction analysis was performed to verify the materials used in the manufacture of the electrodes and possible contamination of the interdigitated electrodes by other metals, which could lead to errors in electrical measurements. Figure 4 shows the diffractogram of the interdigitated electrode and its index peaks.

According to the comparing the sample diffractograms with the standard JCPDS plugs, diffraction peaks similar to two distinct phases were observed on the electrode surface, being: Au⁰ (conductor) and SiO₂ (dielectric substrate).

The metallic gold was deposited on the dielectric substrate surface as a cubic system (space group Fm-3m), with crystallographic peaks at 38.28° (111), 44.42° (200), 64.62° (220), 77.71° (311), and 82.34° (222) [26]. On the other hand, the quartz dielectric substrate (SiO₂) was generated as a hexagonal structure (space group P3121), with crystallographic peaks at 29.31° (100), 30.94° (101), 39.51° (102), 41.52° (111), 42.48° (200), 43.48° (201), 50.15° (112), 59.98° (211), 67.76° (212), 68.16° (203), 79.90° (213), and 81.52° (310).

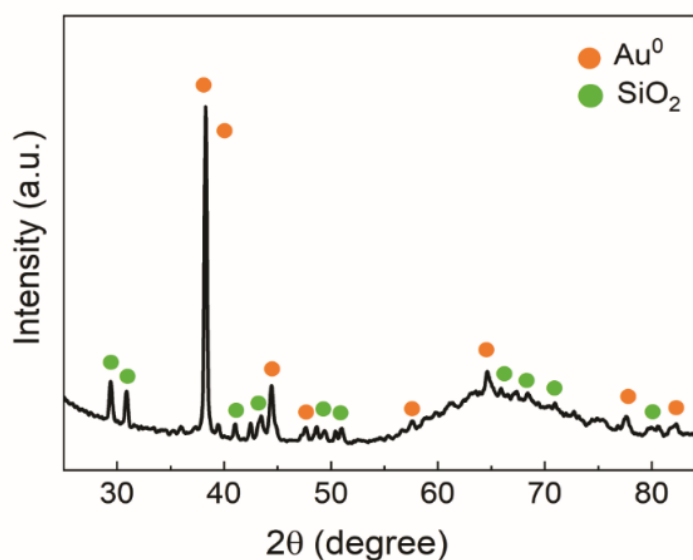


Figure 4. XRD patterns of interdigitated electrodes: Au⁰ (conductor) SiO₂ (dielectric substrate).

During the atomic force microscopy analysis, the deposition of materials was verified, both on the electrode surface (the region between the electrodes) and in the digits (Figure 5). Such material comes from the use of electrodes in samples of pseudo-binary mixtures of biodiesel/diesel.

The geometry of the interdigitated electrode favors the deposition of nanostructures between the digits since the dimensions are reduced. Furthermore, it was also possible to observe irregular edges on the electrodes, possibly related to thin layers' manufacturing process and mechanical stability. Other characteristics observed in the AFM height images are grooves in the region on the thin layer of gold deposited on the quartz substrate. These grooves can best be seen in three-dimensional images, as shown in Figure 5c. These scratches are associated with the gold layer depositing method on the substrate.

The AFM image of the interdigitated electrode shows that the conductive metal tracks were obtained uniformly along the dielectric substrate without major loss of contour.

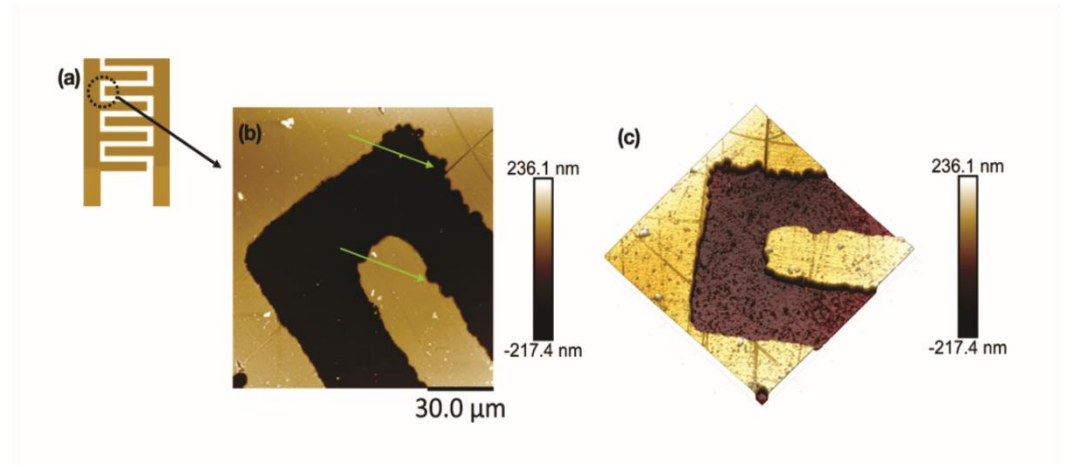
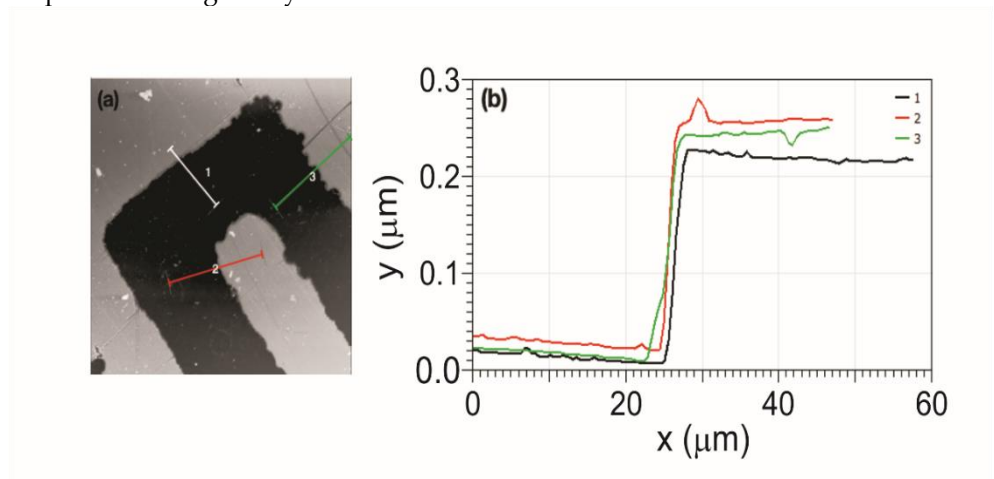


Figure 5. Atomic Force Microscopy topographic image of the interdigital region of the sensor. (a) Schematic figure of the sensor architecture. The AFM image was obtained in the region highlighted by the circle. (b) AFM height image showing the electrode surface and a digit. The green arrows point out defects in the deposited layer. (c) Three-dimensional image corresponding to the image (b). One can observe the grooves on the electrode surface due to the deposition process.

Due to the AFM's ability to acquire three-dimensional images, it was possible to measure the step height of the sensor's gold layer. Several cross sections were obtained, and the mean step value is 225.71 ± 0.0032 nm. Figure 6 shows examples of cross-sectional graphics in three different sensor regions. The steps shown in Figure 6b show a well-defined profile of the gold layer.



From the AFM images, the mean square roughness of the sensor surface was obtained. Three regions were analyzed: the gold layer on the digits, the gold layer on the interdigital region, and the quartz substrate, as illustrated in Figure 7. The area for calculating the roughness over all these regions was $10 \mu\text{m}^2$ and 12 squares were acquired for each region.

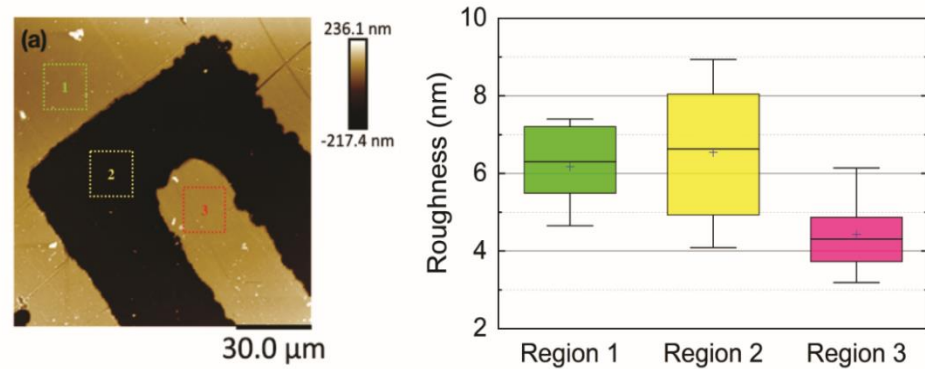


Figure 7. Roughness analysis obtained by Atomic Force Microscopy. (a) AFM topographic image pointing regions in which roughness analysis was performed. Each measure square has $10 \mu\text{m}^2$ and for each region was acquired 12 measurements. Region 1 (green square) corresponds to the sensor surface between the digits, Region 2 (yellow square) corresponds to the sapphire substrate on which the gold layer was deposited and Region 3 (red square) corresponds to the digits surface. (b) Boxplot graphs comparing the roughness values and average for each region. The mean values of quadratic roughness for each region are $6.17 \pm 1.3 \text{ nm}$, $6.54 \pm 1.9 \text{ nm}$ and $4.42 \pm 1.0 \text{ nm}$, respectively, for Region 1, Region 2 and Region 3.

The roughness obtained for Region 1 was $6.17 \pm 1.3 \text{ nm}$, for Region 2 was about $6.54 \pm 1.9 \text{ nm}$ and for Region 3 was $4.42 \pm 1.0 \text{ nm}$. Such roughness differences in each region of the sensor are attributed to the following characteristics: (i) the roughness on the gold surface of the sensor, not corresponding to the digits, has a higher roughness when compared to the fingers, due to the gold deposition process, in this region, the images of AFM reveal several scratches (Figure 5b-c), increasing the roughness. (ii) In the quartz substrate, as shown in the three-dimensional image of the sensor (Figure 5c), as it is a region of depression in the topography, several nanoparticulated residues are trapped there, increasing its roughness value in relation to the sensor body. (iii) In the finger region, the roughness is lower when compared to the other regions, a fact that can be positive, as this is the most important region of the sensor. Although there are differences in the roughness, the whole sensor has nanometric roughness.

According to [27], for applications in electronics, the interdigitated electrodes must have low surface roughness; considering the values obtained, it can be said that the surface of the interdigitated electrodes is suitable for this type of technological application. In addition, this surface can be modified with thin films of conductive materials (conductive polymers), thus, improving its sensitivity and even its selectivity to a certain analyte.

Another AFM investigation was the distribution of adhesion forces on the sensor surface. Figure 8 shows these results. Figure 8a shows the AFM adhesion map on the sensor surface. Analyzing the scale bar shows that the adhesion on the gold surface (purple) is greater than the adhesion on the sapphire substrate (green). The adhesion values were plotted in distribution (Figure 8-red) and Gauss adjusted (black curve). The first Gaussian corresponds to the adhesion values on the sapphire and has a central value of 46.6 nanonewtons. The second Gaussian, corresponding to the gold film, has a value of 57.7 nN. The cumulative frequency graph (blue) shows two regimes, the first achieving saturation (50%) at approximately 50 nN (quartz) and the second at 65 nN (gold) (100%).

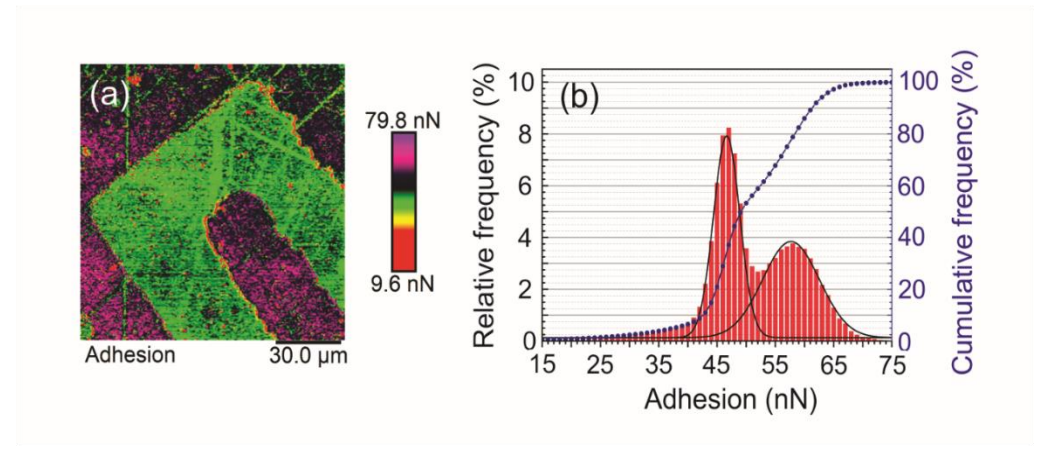


Figure 8. Adhesion analysis obtained by Atomic Force Microscopy. (a) AFM adhesion map over the sensor body. (a) Map shows increase adhesion over the gold layer (purple) when compared with quartz substrate. (b) Adhesion values was plotted as distribution and Gauss fitted. Two distributions can be observed, one correspondent to quartz, and its value is around 46.6 nanonewtons of adhesion force and the other one, correspondent to gold layer, has Gauss distribution around 57.7 nN. The cumulative frequency pointed two regimes, the first one, reaching saturation in approximately 50 nN and the second one in approximately 65 nN.

The scanner microscopy was used for the resolution evaluation of the electrodes. The microscopy images were also a good indicator for the dimensions of the fabricated electrodes and offered information on the electrode quality. In general, all acquired electrodes contained small irregularities that were associated with the microelectronic photolithography method. Figure 9 shows some regions (yellow circle) of the electrode with small defects and irregularities in the digits, in addition to the deposition of particulate materials.

However, no deposition irregularities or defects were observed in any electrode, such as extensive cracks and/or regions with deposition failure, which prevented the use of the electrode; these characteristics guarantee a better distribution of charges electrodes, allowing a large area of interaction with the analyte.

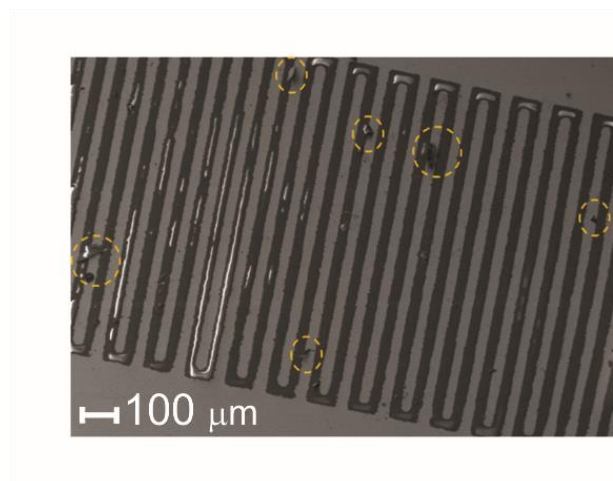


Figure 9. Scanning electron microscopy image of the electrode digit region. The yellow circles show small gaps in the conductive layer

According to [28], to apply interdigitated electrodes such as sensors, biosensors, and even electronic tongue and nose systems, metal electrodes are needed to display precise patterns on their surface, obtained by removing metallic layers, producing the digits. These results indicate that the electrodes obtained by this method were appropriate for

the fabrication of structured devices suitable in biosensors and molecular electronics. However, using lasers with a high repetition rate is an efficient approach to achieve these characteristics and a viable solution to the microelectronic photolithography method, which is a time-consuming and expensive method.

3.3. Electrical characterization

3.3.1. Sensitivity of electrodes to different fuels

Electrodes differentiated by the spacing between digits, as shown in Table 1, were immersed in samples of ethanol, gasoline, diesel, and biodiesel to study their sensitivity. We can see in Figure 10 the capacitance response of the four electrodes differentiated by the spacing between the digits, and we found that the Ba1810 sensor obtained the highest capacitive value for the fuel samples.

However, the capacitive detection of the interdigitated electrode is based on the following equation of permittivity and the relative permittivity of a dielectric material capacitance:

$$C = \frac{\epsilon_0 \times \epsilon_r \times A}{d}, \quad (1)$$

where ϵ_0 and ϵ_r represent vacuum between electrodes, respectively, and where d and A represent electrode distance and area, respectively [27]. Observing the capacitance equation, we can deduce that the smaller the area between the digits, the greater the capacitance of the system; adding the tight distance between combs will maximize the value. This predisposition was also observed in the simulations (Figure 2c).

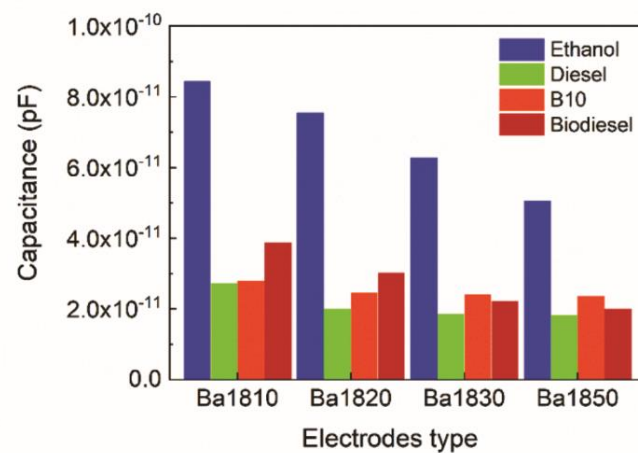


Figure 10. Response of different microelectrode geometries for fuel samples at 1000 Hz and 0.2 V.

Also, the electrodes showed a greater response to ethanol compared to other fuels. As mentioned earlier, this behavior is attributed to biodiesel's values of the dielectric constants, diesel, and gasoline being lower than the dielectric constant of ethanol [28].

It is also interesting to note that the value of the capacitance of the sensor depends on the geometric capacitance between the interdigitated electrodes, the contribution of the glass substrate, and the liquid. According to [29] when the built sensor's capacitive trails are close enough, the field lines act on the entire surface of the sensor, increasing the capacitance of the device.

The edge field effect may be associated with the values obtained in Figure 10, since the interdigitated electrodes are based on this study. It is observed that there is an influence of the electric field in the material that is tested, in this case, hydrated ethanol, fuel, diesel, B10 mixture, and biodiesel. This interaction occurs mainly at the edges of the

capacitor. Thus, the distance between the sensor digits and its angle influences the electric field and, consequently, the capacitance of the system [30].

3.3.1. Sensitivity of electrodes to different fuels

In order to understand the phenomena that occur at the electrode interfaces, impedance spectroscopy measurements were performed. This technique is very useful for the characterization of the electrical behavior of solid or liquid materials (ionic, semiconductor, and dielectric) and electronic devices [31].

Such an experiment aims to differentiate the electrical properties of these media, envisioning the proposition of a method to determine the content of biodiesel and possible contaminants. In this context, the electrical behavior was determined qualitatively for the samples of biodiesel (B100), diesel S10A (B0), and diesel S10B (B10) under the experimental conditions described. We can see in the graphs that the electrodes Ba1810 and Ba1820, represented in Figure 11a and 11b, respectively, had more promising preliminary results since there was a better separation of the curves obtained for each fuel sample.

The spectra consist of well-defined semicircles, each of which could be ideally assembled using an equivalent circuit consisting of a parallel resistance-capacitance network. The semicircle corresponds to the process of electron transfer at high frequencies. On the left side of the semicircle, the impedance of the system is dominated by the resistance of the solution (R_s). On the right side, in the region of low frequencies, the impedance of the system is dominated by the sum of the solution resistance and the load transfer resistance (R_{ct}) [34,35]. According to [34] the R_{ct} is mainly affected by the kinetics of electron transfer from the electrolyte to the metal and depends on the properties concentration of species, temperature, applied potential and, the structure of the interface.

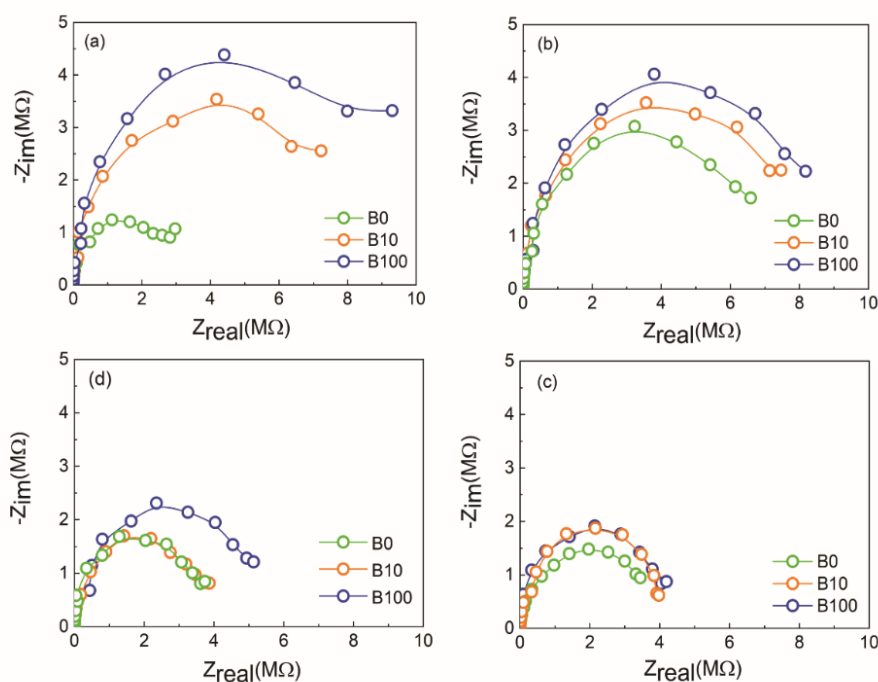


Figure 11. Nyquist diagrams of the fuel samples, using the electrodes: (a) Ba1810, (b) Ba1820, (c) Ba1830 and (d) Ba1850.

As shown in Figure 11, the impedance values of biodiesel, diesel, and the B10 mixture are in megaohms, indicating a very high electrical resistance of the liquid. According to [37,38], these values align with the expected values for viscous and non-polar liquids.

Similar impedance values of gigaohms and even teraohms are observed for biodiesel fuels and mixtures [37].

We also see in Figure 11, more precisely in the region of low frequencies, the tendency of forming a second capacitive arc is more evident in samples of B100 than for the media where there is the presence of diesel, indicating a possible interaction of biodiesel with the surface of the electrode. This fact was also observed by [38]. Furthermore, it can be seen that the value of load transfer resistance for B0 is lower when compared to B10, which has 10 % biofuel and B100, demonstrating in principle that the first is a more conductive medium when compared with the last two.

Moreover, Figure 11 suggests that the addition of biodiesel increases the conduction processes in Diesel/Biodiesel mixtures. According to [39], monitoring the dielectric constant of the materials (calculated from capacitance) is more promising to assess the biodiesel content in mixtures Diesel/Biodiesel than the use of resistivity measures.

As shown in Figure 12, the impedance of the fuel sample declined with increasing signal frequency, especially in the range higher than 100 Hz. However, in the high-frequency region, the differences in the values of the impedimetric signals between the fuels with different blending ratios are not significant. Nevertheless, in the low-frequency region from 100 to 1 Hz, there are apparent impedimetric differences in discriminating and estimating biodiesel's blending ratio.

Analyzing the Bode diagram, Figure 12 shows that the addition of a fixed volume of biodiesel in the cell causes a shift in the impedance value in the low-frequency region to even greater values. According to [40], biodiesel may be interacting with the metallic surface, thus contributing to the formation of this insulating film and thus hampering the passage of electrical current at the interface. This behavior can also be observed in Diesel S10A. It is believed that such behavior may be related to accumulations of organic species present in this medium and the presence of sulfur [41].

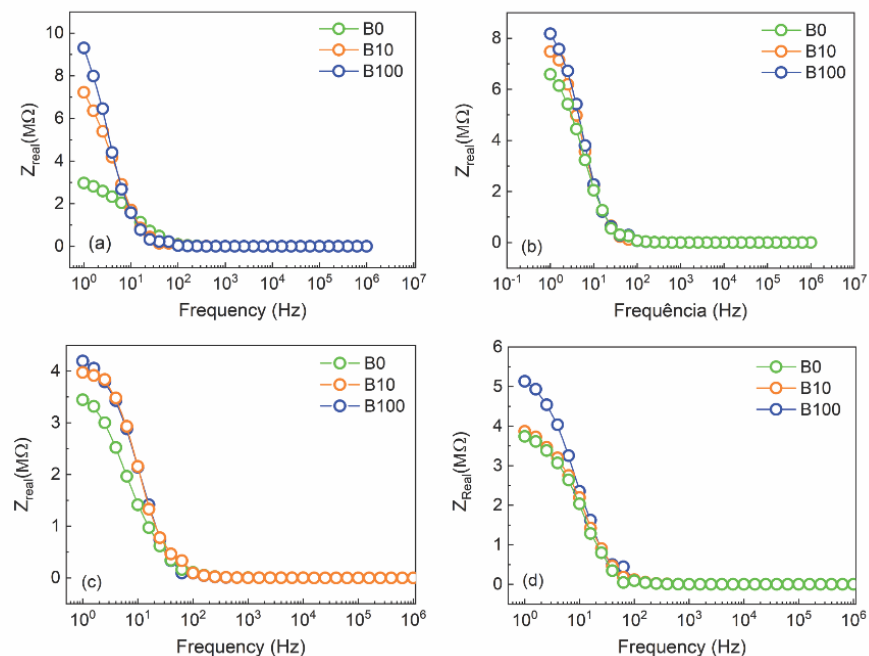


Figure 12. Bode diagram of the fuel samples, using the electrodes: a) Ba1810, b) Ba1820, c) Ba1830 and d) Ba1850.

An equivalent circuit for the studied systems was proposed to interpret the results shown above, shown in Figure 13. The circuit is formed by a resistor (R1) in series with a parallel arrangement of a constant phase element (CPE1) with the resistance (R2) that is in series with the constant phase element (CPE2). We can observe capacitances at low frequencies, represented by a constant phase element (CPE) in the circuit, possibly due to an irregularity in the metallic surface, making it difficult for current to pass. The values for each parameter can be seen in Table 2. All components are verified by the chi-square evaluation, with a 95% confidence level.

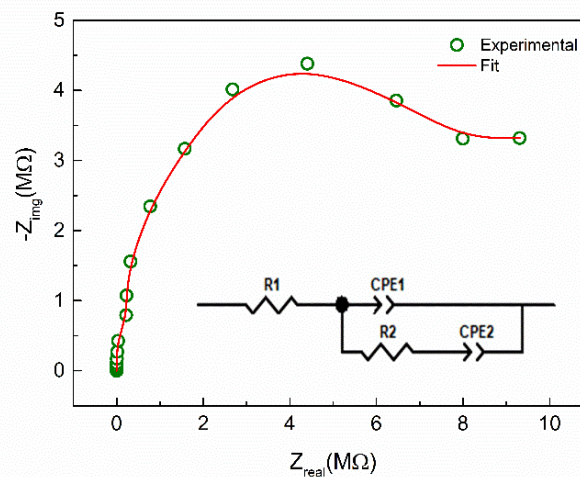


Figure 13. Adjustment of the proposed equivalent circuit for the pseudo-binary mixture of biodiesel/diesel.

Circuit element	Value	Error (%)	χ^2
R1 (MΩ)	4035	3,652	0,003
CPE1 (pF)	0,986	0,002	
R2 (MΩ)	$8,816 \times 10^9$	2,674	
CPE2 (pF)	4,345	0,181	

After studying the electrical properties of the pseudo-binary mixtures and the results obtained using the equivalent electrical circuit, we realized that the samples of pseudo-binary blends followed the same pattern of equivalent circuit observed in Figure 13. We also found that the resistance value of load transfer (R2) increased with the addition of biodiesel to the system, showing that the value of (R2) is dependent on the presence of biodiesel in the system. A similar result was presented [42].

4. Discussion

This section aims to identify possible reasons for the observed change in the dielectric properties of samples of biodiesel/diesel pseudo-binary mixtures, referring to previous research work. This investigation associates the capacitance values obtained in the simulations to define the best architecture of interdigitated electrodes, in addition to the characterizations (morphological, structural, and electrical) in the manufactured electrodes.

The performance of a capacitive sensor, signal strength, depth of penetration, and metrological sensitivity are mainly connected to sensor geometry. A 3D electrostatic simulation based on finite element methods was used to determine the topology of

interdigitated electrodes to be manufactured since the ability to measure analytes depends on the topology of the electrode. Based on the modeling performed, it can be assumed that the geometric parameters more suitable for the construction of the electrode are: $W = 20 \mu\text{m}$, $L = 1000 \mu\text{m}$, $G = 50 \mu\text{m}$ e $N = 40$ digits.

Further, it was possible to demonstrate the effects of the electric field between the electrode digits. It was observed that under certain conditions, the magnitude of the electric field is greater among the electrodes with less spacing between the digits Figure 3. According to [43] the magnitude of the electric field above the interdigitated electrodes is proportional to the spacing between the digits. Also, it depends on changes in the dielectric properties of the materials.

Also, in Figure 3, we can observe the electric field's penetration depth, which can be defined as the maximum distance in the z-direction for the sensor to produce a detectable change in the sensor output (capacitive planar sensor). According to [44], it is an important parameter to indicate how far the sensor can be sensitive, be determined by the permittiveness of the material and the geometry of the electrode. In this context, we observe in Figure 3 that although the electrode with the largest conductive layer has a greater capacitance than the one with the lowest conductive layer, the depth of penetration of the electric field is practically the same.

Regarding the structural characterization by X-ray diffraction Figure 4, it was possible to observe peaks of diffraction similar to two distinct phases on the surface of the electrodes, being: Au^0 (conductor) and SiO_2 (dielectric substrate), it is not possible to verify the added chromium layer to promote greater adherence of gold to the substrate.

Concerning the depth of the devices in Figure 5 and Figure 6, it was possible to observe that the electrodes have a gold conductive layer of $225.71 \pm 0.0032 \text{ nm}$.

Although differences in roughness have been observed due to the gold deposition process, scratches in the conductive layer, and nanoparticulate residues, the entire sensor has nanometric roughness, Figure 7.

The distribution of adhesion forces on the sensor surface, Figure 8, was also assessed; this study is important because fuel molecules must attach to the surface of the sensor – no problems for eventual surface modification, to promote greater sensitivity to the analyte of interest.

In scanning electron microscopy Figure 9 of the electrodes, it was possible to verify some irregularities on the surface and edges attributed to the microelectronic photolithography method. These imperfections could be corrected using the laser ablation method.

The sensitivity of the interdigitated electrodes was also investigated and showed that the manufactured devices with lesser spacing between the combs (Ba1810 and Ba1820) showed greater sensitivity to fuels, as can be seen in Figure 10. Furthermore, the electrodes showed a greater response to ethanol than other fuels. As mentioned earlier, this behavior is attributed to biodiesel's values of the dielectric constants, diesel, and gasoline being lower than the dielectric constant of ethanol.

The electrical behavior observed in the Nyquist diagram Figure 11 is characterized by a capacitive arc and in the low-frequency region, another behavior that can be attributed to interfacial phenomena [45,46]. It was also possible to observe a loss of sensitivity in medium and high-frequency regions, making it possible to distinguish between fuels in the low-frequency region, as shown in Figure 12.

In the equivalent circuit Figure 13, we observe the resistance (R_1) comes from the species present in the pseudo-binary biodiesel/diesel mixture; that is, it is the resistance of the solution. The metal interface with the mixture is represented by the resistance (R_2), featuring a load transfer resistance. The double-layer capacitance is represented by (CPE_1) and (CPE_2) related to insulating film formed on the surface in this type of electrode. Thus, reinforcing the hypothesis of forming a capacitive film on the metal surface of the electrode. The method is reliable and indicates good analytical performance because it presented small errors between the experimental and simulated data (Table 2).

After studying the electrical properties, we found that the value of the load transfer resistance (R_2) increased with the addition of biodiesel to the system. In this context, we can attribute that the value of (R_2) depends on biodiesel in the system.

Future work should focus on further optimization of conditions to maximize results and develop a device that measures the spot, giving an estimate of the quality of the fuel.

5. Conclusions

In this paper, simulations were used to determine the topology and ideal conditions for using interdigitated electrodes as fuel sensors.

The electrical characterization results show that it is possible to differentiate the fuels and determine the biodiesel content in the diesel in the low-frequency region by using the developed electrodes. The analytical method also provides data that might be used in other applications, such as resolving the adulteration or purity of biofuel. It is worth mentioning that the proposed method has a lower cost when compared to the official methodology adopted by the National Petroleum Agency, natural gas and bio-fuels - ANP (EN 14078 and NBR 15568).

Author Contributions: For research articles with several authors, a short paragraph specifying their individual contributions must be provided. The following statements should be used “Conceptualization, A.B. and F.S.; methodology, I.S.N., C.A., G.F.; validation, I.S.N. and G.F.; formal analysis, F.S., A.B., J.F.N; investigation, I.S.N. and V.P.; data curation, I.S.N. and C.C.; writing—original draft preparation, I.S.N. and F.S; writing—review and editing, L.A. and F.S. All authors have read and agreed to the published version of the manuscript.” Please turn to the CRediT taxonomy for the term explanation. Authorship must be limited to those who have contributed substantially to the work reported.

Funding: The authors gratefully acknowledge financial support from FAPEMA, CAPES and CNPq.

Acknowledgments: The authors thank the ODFJELL TERMINALS GRANEL QUÍMICA LTDA and UNICONTROL BRASIL

Conflicts of Interest: The authors declare no conflict of interest.

References

1. Borges, M.E.; Díaz, L. Recent developments on heterogeneous catalysts for biodiesel production by oil esterification and transesterification reactions: A review. *Renew. Sustain. Energy Rev.* **2012**, *16*, 2839–2849.
2. Da Costa, R.P.M.; Khalila, T.C.; Dos Santos, A.P.F.; De Andrade, D.F.; D’Avila, L.A. Determinação do teor de biodiesel em diesel empregando o ensaio colorimétrico do ácido hidroxâmico. *Quim. Nova* **2015**, *38*, 563–569.
3. Scherer, M.D.; Oliveira, S.L.; Lima, S.M.; Andrade, L.H.C.; Caires, A.R.L. Determination of the biodiesel content in diesel/biodiesel blends: A method based on fluorescence spectroscopy. *J. Fluoresc.* **2011**, *21*, 1027–1031.
4. Faria, R.C.M.; Rezende, M.J.C.; Rezende, C.M.; Pinto, A.C. Desenvolvimento e validação de metodologia de análise de misturas biodiesel: Diesel utilizando cromatografia gasosa-espectrometria de massas. *Quim. Nova* **2007**, *30*, 1900–1905.
5. Oliveira, F.C.C.; Brandão, C.R.R.; Ramalho, H.F.; da Costa, L.A.F.; Suarez, P.A.Z.; Rubim, J.C. Adulteration of diesel/biodiesel blends by vegetable oil as determined by Fourier transform (FT) near infrared spectrometry and FT-Raman spectroscopy. *Anal. Chim. Acta* **2007**, *587*, 194–199.
6. Diniz Carvalho, C.; Barros, A.K.; Lopes, M.V.; Silva, F.C.; Santana, E.E.; Sinfrônio, F.S.M. Determination of the composition of biodiesel-diesel blends using the dielectric constant. *Instrum. Sci. Technol.* **2016**, *44*, 377–385.
7. Kutia, M.; Mukhin, N.; Petrova, H.; Oseev, A.; Bakhchova, L.; Schmidt, M.P.; Aman, A.; Palis, S.; Tarasov, S.;

- Hirsch, S. Sensor for the evaluation of dielectric properties of sulfur-containing heteroatomic hydrocarbon compounds in petroleum based liquids at a microfluidic scale. *AIP Adv.* **2020**, *10*.
8. González Prieto, L.E.; Sorichetti, P.A.; Romano, S.D. Electric properties of biodiesel in the range from 20 Hz to 20 MHz. Comparison with diesel fossil fuel. *Int. J. Hydrogen Energy* **2008**, *33*, 3531–3537.
 9. Yule, A.J.; Shrimpton, J.S.; Watkins, A.P.; Balachandran, W.; Hu, D. Electrostatically atomized hydrocarbon sprays. *Fuel* **1995**, *74*, 1094–1103.
 10. Us, A.; Koehler, C.; Seitz, M.; Wooton, D. Patentes Espectroscopia de impedância (is) métodos e sistemas para caracterizar combustível. **2018**, 1–9.
 11. Bueno, L.; Paixão, T.R.L.C. A copper interdigitated electrode and chemometrical tools used for the discrimination of the adulteration of ethanol fuel with water. *Talanta* **2011**, *87*, 210–215.
 12. Rocha-Gaso, M.-I.; March-Iborra, C.; Montoya-Baides, Á.; Arnau-Vives, A. Surface Generated Acoustic Wave Biosensors for the Detection of Pathogens: A Review. *Sensors* **2009**, *9*, 5740–5769.
 13. Ramli, N.A.; Nordin, A.N. Design and modeling of MEMS SAW resonator on Lithium Niobate. *2011 4th Int. Conf. Mechatronics Integr. Eng. Ind. Soc. Dev. ICOM'11 - Conf. Proc.* **2011**, 1–4.
 14. Mahameed, R.; El-Tanani, M.A.; Rebeiz, G.M. A zipper RF MEMS tunable capacitor with interdigitated RF and actuation electrodes. *J. Micromechanics Microengineering* **2010**, *20*.
 15. Vakilian, M.; Majlis, B.Y. Study of interdigitated electrode sensor for lab-on-chip applications. *IEEE Int. Conf. Semicond. Electron. Proceedings, ICSE* **2014**, 201–204.
 16. Qureshi, A.; Niazi, J.H.; Kallemudi, S.; Gurbuz, Y. Label-free capacitive biosensor for sensitive detection of multiple biomarkers using gold interdigitated capacitor arrays. *Biosens. Bioelectron.* **2010**, *25*, 2318–2323.
 17. Valera, E.; Ramón-Azcón, J.; Sanchez, F.J.; Marco, M.P.; Rodríguez, Á. Conductimetric immunosensor for atrazine detection based on antibodies labelled with gold nanoparticles. *Sensors Actuators, B Chem.* **2008**, *134*, 95–103.
 18. Ding, S. Highly sensitive biosensors with interdigitated electrode arrays Title. **2018**, 89.
 19. Ding, S.; Mosher, C.; Lee, X.Y.; Das, S.R.; Cargill, A.A.; Tang, X.; Chen, B.; McLamore, E.S.; Gomes, C.; Hostetter, J.M.; et al. Rapid and Label-Free Detection of Interferon Gamma via an Electrochemical Aptasensor Comprising a Ternary Surface Monolayer on a Gold Interdigitated Electrode Array. *ACS Sensors* **2017**, *2*, 210–217.
 20. Rivadeneyra, A.; Fernández-Salmerón, J.; Agudo-Acemel, M.; López-Villanueva, J.A.; Capitan-Vallvey, L.F.; Palma, A.J. Printed electrodes structures as capacitive humidity sensors: A comparison. *Sensors Actuators, A Phys.* **2016**, *244*, 56–65.
 21. Bowen, C.R.; Bowles, A.; Drake, S.; Johnson, N.; Mahon, S. Fabrication and finite element modelling of interdigitated electrodes. *Ferroelectrics* **1999**, *228*, 257–269.
 22. Mizuguchi, J.; Piai, J.C.; De França, J.A.; De Moraes França, M.B.; Yamashita, K.; Mathias, L.C. Fringing field capacitive sensor for measuring soil water content: Design, manufacture, and testing. *IEEE Trans. Instrum. Meas.* **2015**, *64*, 212–220.
 23. Wang, Y.; Chong, N.; Cheng, Y.L.; Chan, H.L.W.; Choy, C.L. Dependence of capacitance on electrode configuration for ferroelectric films with interdigital electrodes. In *Proceedings of the Microelectronic Engineering*; 2003.
 24. Han, T.; Nag, A.; Simorangkir, R.B.V.B.; Afsarimanesh, N.; Liu, H.; Mukhopadhyay, S.C.; Xu, Y.; Zhadobov, M.; Sauleau, R. Multifunctional flexible sensor based on laser-induced graphene. *Sensors (Switzerland)* **2019**, *19*, 13–22.
 25. Bilican, I.; Guler, M.T.; Gulener, N.; Yuksel, M.; Agan, S. Capacitive solvent sensing with interdigitated microelectrodes. *Microsyst. Technol.* **2016**, *22*, 659–668.
 26. Colniță, A.; Marconi, D.; Turcu, I. Fabrication of Interdigitated Electrodes using Molecular Beam Epitaxy and Optical Lithography. *Anal. Lett.* **2016**, *49*, 378–386.

27. Jung, H.W.; Chang, Y.W.; Lee, G. yeon; Cho, S.; Kang, M.J.; Pyun, J.C. A capacitive biosensor based on an interdigitated electrode with nanoislands. *Anal. Chim. Acta* **2014**, *844*, 27–34.
28. Wiziack, N.K.L. Desenvolvimento De Sistemas Multissensoriais Híbridos , Língua E Narizes Eletrônicos Para a Desenvolvimento De Sistemas Multissensoriais Híbridos , Língua E Narizes Eletrônicos Para a. *Tese doutorado* **2010**, USP.
29. Mizuguchi, J. Sensores Capacitivos por Efeito do Campo de Borda Aplicados a Quantificação do Molhamento Foliar e da Agua Presente no Solo. **2014**, 120.
30. Dean, R.N.; Rane, A.K.; Baginski, M.E.; Richard, J.; Hartzog, Z.; Elton, D.J. A capacitive fringing field sensor design for moisture measurement based on printed circuit board technology. *IEEE Trans. Instrum. Meas.* **2012**, *61*, 1105–1112.
31. Hirschorn, B.; Orazem, M.E.; Tribollet, B.; Vivier, V.; Frateur, I.; Musiani, M. Determination of effective capacitance and film thickness from constant-phase-element parameters. *Electrochim. Acta* **2010**, *55*, 6218–6227.
32. Rahmawati; Djatna, T.; Noor, E.; Irzaman An identification and characterization of biodiesel fatty acid based by using dielectric sensor. *IOP Conf. Ser. Earth Environ. Sci.* **2017**, *65*.
33. Pereira, T.C.; Delfino, J.R.; Ferreira, A.A.P.; Barros, F.J.S.; Marques, E.P.; Zhang, J.; Marques, A.L.B. Stainless Steel Electrodes to Determine Biodiesel Content in Petroleum Diesel Fuel by Electrochemical Impedance Spectroscopy. *Electroanalysis* **2017**, *29*, 814–820.
34. Brosel-Oliu, S.; Abramova, N.; Uria, N.; Bratov, A. Impedimetric transducers based on interdigitated electrode arrays for bacterial detection – A review. *Anal. Chim. Acta* **2019**, *1088*, 1–19.
35. Bocian, P.; Biernat, K.; Matuszewska, A.; Sharma, P.S.; Bukrejewski, P.; Noworyta, K.R. Electrochemical impedance spectroscopy studies of gasoline oxidative stability – Attempt to devise new gasolines chemical stability index. *Fuel* **2021**, *288*.
36. Biernat, K.; Bocian, P.; Bukrejewski, P.; Noworyta, K.R. Application of the impedance spectroscopy as a new tool for studying biodiesel fuel aging processes. *Energies* **2019**, *12*, 1–12.
37. Ulrich, C.; Petersson, H.; Sundgren, H.; Björefors, F.; Krantz-Rülcker, C. Simultaneous estimation of soot and diesel contamination in engine oil using electrochemical impedance spectroscopy. *Sensors Actuators, B Chem.* **2007**, *127*, 613–618.
38. Delfino, J.R.; Pereira, T.C.; Costa Viegas, H.D.; Marques, E.P.; Pupim Ferreira, A.A.; Zhang, L.; Zhang, J.; Brandes Marques, A.L. A simple and fast method to determine water content in biodiesel by electrochemical impedance spectroscopy. *Talanta* **2018**, *179*, 753–759.
39. De Souza, J.E.; Scherer, M.D.; Cáceres, J.A.S.; Caires, A.R.L.; M’Peko, J.C. A close dielectric spectroscopic analysis of diesel/biodiesel blends and potential dielectric approaches for biodiesel content assessment. *Fuel* **2013**, *105*, 705–710.
40. Pereira, F. Espectroscopia de impedância aplicada à caracterização de células parasitadas numa plataforma de microfluídica. **2012**, 127.
41. Lvovich, V.F.; Liu, C.C.; Smiechowski, M.F. Optimization and fabrication of planar interdigitated impedance sensors for highly resistive non-aqueous industrial fluids. *Sensors Actuators, B Chem.* **2006**, *119*, 490–496.
42. Davanse, L.G. Aplicação de espectroscopia de impedância no estudo de blendas de biodiesel / diesel, UNIVERSIDADE ESTADUAL DE MARINGÁ, 2010.
43. Mamishev, A. V.; Sundara-Rajan, K.; Yang, F.; Du, Y.; Zahn, M. Interdigital sensors and transducers. *Proc. IEEE* **2004**, *92*, 808–844.

-
44. Abdollahi, F.; Savard, S.; Maldague, X.; Filleter, T.; Bendada, A.H. NON-DESTRUCTIVE TESTING OF MATERIALS BY CAPACITIVE SENSING. 1–7.
 45. Pajkossy, T.; Jurczakowski, R. Electrochemical impedance spectroscopy in interfacial studies. *Curr. Opin. Electrochem.* **2017**, *1*, 53–58.
 46. Jafari, H.; Idris, M.H.; Ourdjini, A.; Rahimi, H.; Ghobadian, B. EIS study of corrosion behavior of metallic materials in ethanol blended gasoline containing water as a contaminant. *Fuel* **2011**, *90*, 1181–1187.